

AbsGS: Recovering Fine Details for 3D Gaussian Splatting

Zongxin Ye*
National University of Defense
Technology
Changsha, China
yezongxin21@nudt.edu.cn

Wenyu Li*
National University of Defense
Technology
Changsha, China
wenyu18@nudt.edu.cn

Sidun Liu
National University of Defense
Technology
Changsha, China
liusidun@nudt.edu.cn

Peng Qiao
National University of Defense
Technology
Changsha, China
pengqiao@nudt.edu.cn

Yong Dou
National University of Defense
Technology
Changsha, China
yongdou@nudt.edu.cn

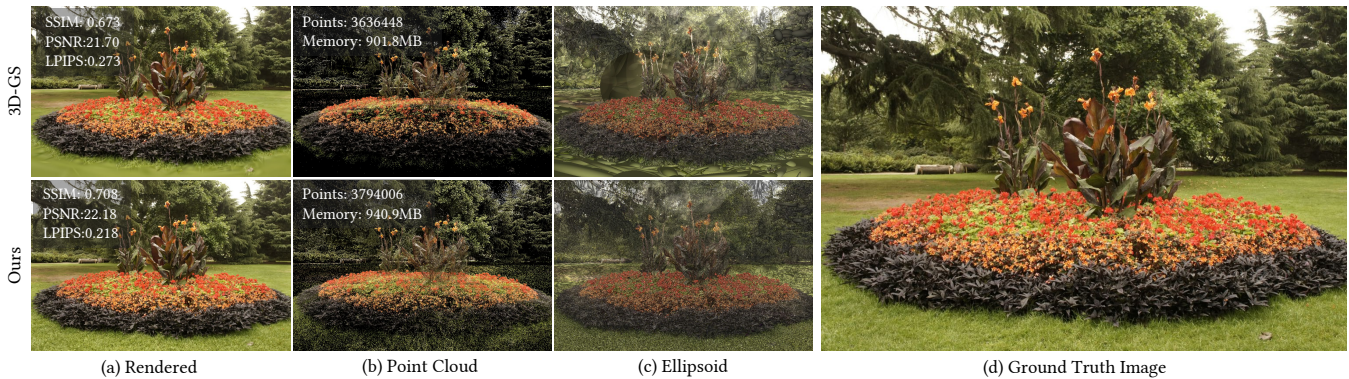


Figure 1: We reveal that the original adaptive density control strategy in 3D Gaussian Splatting (3D-GS) has the flaw of gradient collision which results in degradation, and propose homodirectional gradient as the guidance for densification. (a) Our method recovers fine details and achieves higher quality novel view synthesis results. SSIM, PSNR, LPIPS are inset. (b) Our proposed method yields more reasonable distribution of Gaussian points with comparable number of Gaussians and memory consumption with 3D-GS. (c) By adopting our method, the large Gaussians in over-reconstructed regions that lead to blur are eliminated.

ABSTRACT

3D Gaussian Splatting (3D-GS) technique couples 3D Gaussian primitives with differentiable rasterization to achieve high-quality novel view synthesis results while providing advanced real-time rendering performance. However, due to the flaw of its adaptive density control strategy in 3D-GS, it frequently suffers from over-reconstruction issue in intricate scenes containing high-frequency details, leading to blurry rendered images. The underlying reason for the flaw has still been under-explored. In this work, we present a comprehensive analysis of the cause of aforementioned artifacts, namely gradient collision, which prevents large Gaussians in over-reconstructed regions from splitting. To address this issue, we propose the novel homodirectional view-space positional gradient as the criterion for densification. Our strategy efficiently identifies large Gaussians in over-reconstructed regions, and recovers fine details by splitting. We evaluate our proposed method on various challenging datasets. The experimental results indicate that our approach achieves the best rendering quality with reduced or similar memory consumption. Our method is easy to

implement and can be incorporated into a wide variety of most recent Gaussian Splatting-based methods. We will open source our codes upon formal publication. Our project page is available at: <https://ty424.github.io/AbsGS.github.io/>

KEYWORDS

Novel View Synthesis, 3D Gaussian Splatting, Point-based Radiance Field, 3D reconstruction

1 INTRODUCTION

High quality novel view synthesis from multiple unordered images is a long-standing problem for 3D vision researchers. Recent advances on neural rendering have revolutionized this task by learning a neural implicit representation instead of explicit point clouds or meshes. One of the most effective approach with in this paradigm has been reconstructing a set of 3D Gaussian primitives of the scene[17]. Coupled with splat-based rasterization, 3D Gaussian Splatting (3D-GS)[17] produces compelling real-time rendering results with unprecedented fidelity. The remarkable performance of 3D-GS is closely tied to the adaptive density control

* Both authors contributed equally to this research.

strategy. Initialized solely from a set of sparse point clouds derived from Structure from Motion (SfM), 3D-GS gradually populate empty areas by split/cloning existing Gaussians, ultimately covering whole scenes with compact and precise representation. There have been many interests on extending 3D-GS to other applications, e.g., dynamic modeling[9, 29, 37, 42], single-view or text-to-view generation[30, 39, 43, 44], mesh extraction[12, 15, 32], SLAM[8, 14, 40] and so on.

However, applying 3D Gaussian Splatting to complex scenes encounters the issue of over-reconstruction, where regions containing high frequency details are covered by only a small number of large Gaussians. Consequently, the rendering results become blurry and cannot accurately reflect the appearance and geometry of the scene as validated in Fig. 1. The cause of over-reconstruction is that the adaptive density control strategy cannot effectively identify large Gaussians in over-reconstructed areas and split them to represent details. The deficiency of the strategy has not been well explored.

In this paper, we find that the deficiency of the original strategy lies in its failure to consider the negative impact of pixel-wise sub-gradient directions on the identification of large Gaussians in over-reconstructed areas. Specifically, original 3D-GS proposes to use the view-space positional gradient to determine whether if a large Gaussian requires split. We observe that for each Gaussian primitive the pixel-wise sub-gradients of the view-space positional gradient may have different directions. Therefore, the sub-gradients cancel each other out during the process of summation, namely *gradient collision*. Especially for large Gaussians covering many pixels, maintaining consistent gradient directions for each pixel becomes exceptionally challenging which results in a small-scale view-space positional gradient. Consequently, the magnitude of view-space positional gradient fails to surpass the densification threshold, thereby hindering the split of over-reconstructed Gaussians.

Based on the above analysis, we propose homodirectional view-space positional gradient as criteria for densification. Homodirectional view-space positional gradient is designed as the sum of the absolute values of pixel-wise sub-gradients covered by a Gaussian primitive, based on the rationale that the representation quality is solely dependent on the magnitude of the gradient, irrespective of its direction. The absolute operation can mitigate the influence of gradient direction while retaining the influence of gradient magnitude. The homodirectional view-space positional gradient therefore avoids the gradient collision and facilitates the split of large Gaussians in over-reconstructed regions that were unrecognized by original strategy. An overview of our method (dubbed as AbsGS) is shown in Fig. 2.

We evaluate AbsGS on previously published real-world datasets. The experiment results show that our method consistently yields high quality novel view synthesis and exhibits better results on PSNR, SSIM, and LPIPS. At the same time, our method keeps similar or less memory consumption compared with 3D-GS. From the visualization of Gaussian ellipsoids, we observe that our method eliminates over-reconstruction areas and recovers fine details while 3D-GS fails and leads to blur, as illustrated in Fig. 1. In summary, our contributions are as follows:

- First, we analyze the deficiency of the original strategy that results in over-reconstruction is caused by gradient collision.

- Second, a straightforward yet effective strategy is proposed to utilize homodirectional view-space positional gradient as guidance for densification throughout training.
- Third, our proposed method can effectively eliminate large Gaussians in over-reconstructed regions, and achieves better novel view synthesis quality with similar or less memory consumption.

2 RELATED WORKS

Neural Implicit 3D Representation. In contrast to widely adopted classic explicit 3D representation, e.g., point cloud, voxels and mesh, more recent learning-based neural implicit representations do not require complex regularization, attract more attention and achieve more accurate rendering results. As a revolutionary pioneer, Neural Radiance Fields (NeRF)[20] couples differentiable ray-marching with continuous radiance field to enable end-to-end optimization from images. NeRF has been broadly receiving massive interest towards more photo-realistic novel view synthesis[1, 2, 4] and its follow-up methods have been providing impressive results to other applications, e.g., dynamic modeling[11, 24, 25], surface reconstruction[35, 36, 38, 41], 3D asset generation[16, 26, 34]. However, with expensive volumetric ray-marching which densely sample point locations along the camera rays, NeRF is inefficient for training at the beginning of design. Though notable NeRF-variants [5, 10, 21, 27] have been proposed to alleviate the training/inference computation burden by introducing spatial datastructures to store neural features instead of large MLPs, the plenty of sampling and queries can not be avoided due to the inherent requirement of volumetric rendering. Instead, point based representations with learnable attributes support more efficient forward rasterization for real-time rendering. More recently, 3D Gaussian Splatting (3D-GS)[17], revisit fast point-based rendering engine with learnable Gaussian primitives. Starting from initial sparse point clouds from Structure from Motion (SfM)[23, 28, 33], the optimization procedure moves the Gaussians to correct positions, creates new Gaussians to cover empty space, removes invalid Gaussians and finally produces a set of Gaussians to precisely represent underlying scenes. As an unstructured and discrete representation that supports forward rasterization, it fundamentally avoid the shortcomings of expensive sampling and queries and provide real-time rendering performance, along with high quality for novel-view synthesis. Nowadays there have been many subsequent extensions of 3D Gaussian splatting, e.g., surface reconstruction[6, 12, 15], generation[7, 22, 31, 39] and dynamic modeling[19, 37].

3 METHOD

In this section, we first review the basic background of 3D-GS in Section 3.1; then, we describe the gradient collision phenomenon that prevent large Gaussians in over-reconstructed regions from splitting in Section 3.2; finally, we propose the homodirectional gradient as guidance for splitting and present the details in Section 3.3.

3.1 Preliminary

3D Gaussian Splatting (3D-GS)[17] proposes to represent scenes by a set of learnable 3D Gaussians G_0, G_1, \dots, G_N . Each 3D Gaussian primitive G_i is explicitly parameterized via center position μ_i^{3d} and

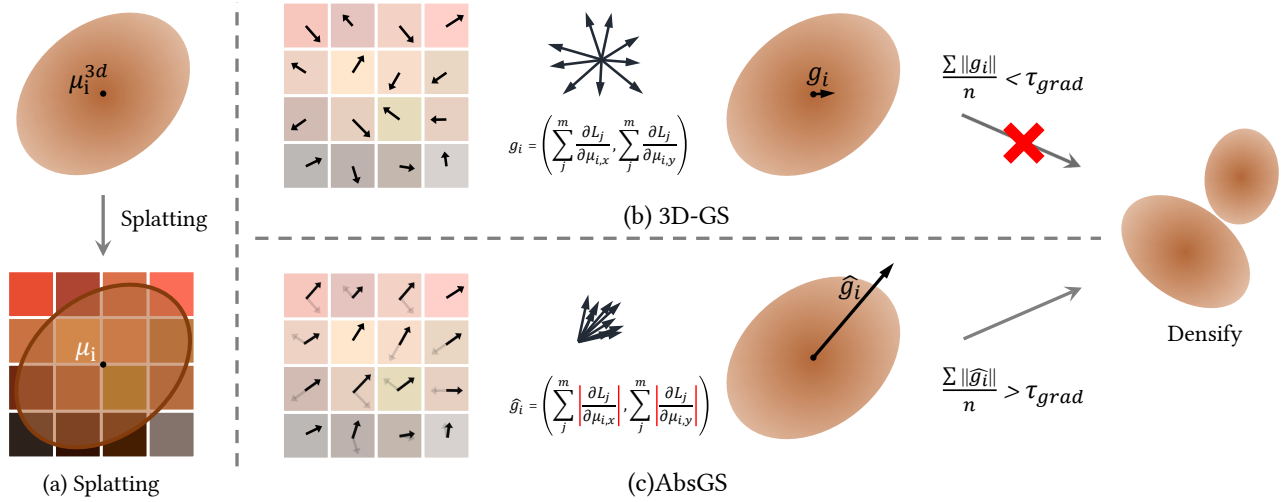


Figure 2: Overview of our method. (a) The splat-based rendering technique project Gaussian G_i with mean position μ_i^{3d} to 2D coordinate μ_i in pixel-space. The number of covered pixels by Gaussian G_i is m . (b) By backpropagating, the view-space gradient g_i of Gaussian G_i under viewpoint k is calculated as the sum of all view-space gradients of pixels that are covered by G_i . Since the gradients $\frac{\partial L_j}{\partial \mu_i}$ have different directions, the overall sum g_i will have a small scale, which do not satisfy the gradient threshold for densification. (c) Motivated by above analysis, we redesign densitification scheme by taking the absolute value of each component $|\frac{\partial L_j}{\partial \mu_{i,x}}|$ and $|\frac{\partial L_j}{\partial \mu_{i,y}}|$ before summing. This enables to identify large Gaussians in over-reconstructed regions for split.

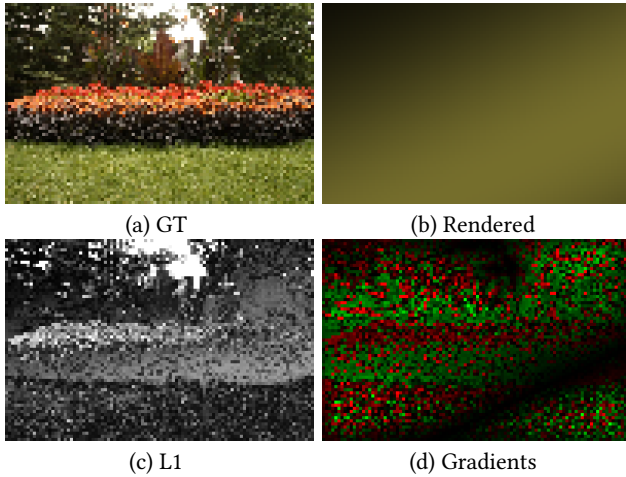


Figure 3: We analyze gradient collision for view-space positional gradient, by optimizing single Gaussian to fit a image. We show the x-axis direction of pixel-wise gradient in (d), where red represents positive and green represents negative.

full 3D covariance matrix Σ_i^{3d} :

$$G_i(x) = e^{-\frac{1}{2}(x-\mu_i^{3d})^T(\Sigma_i^{3d})^{-1}(x-\mu_i^{3d})} \quad (1)$$

3D Gaussian primitive also has two additional learnable attributes: opacity o_i and spherical harmonics coefficients SH_i to model view dependent color. To render an image, the 3D Gaussian primitive G_i

is first transformed into the camera coordinate and projected onto image plane, resulting the 2D Gaussian G_i^{2d} with center position μ_i and 2D covariance matrix Σ_i^{2d} :

$$G_i^{2d}(x) = e^{-\frac{1}{2}(x-\mu_i)^T(\Sigma_i^{2d})^{-1}(x-\mu_i)} \quad (2)$$

then differentiable alpha blending is employed to integrate colors from front-to-back:

$$c(x) = \sum_i^N c_i \alpha_i \prod_{j=1}^{i-1} (1 - \alpha_j) \quad (3)$$

$$\alpha_i = \sigma(o_i) \times G_i^{2d}(x) \quad (4)$$

where $\sigma(\cdot)$ is the sigmoid function and N is the number of Gaussians that participate in alpha blending. 3D-GS initializes 3D Gaussians with the free sparse point clouds produced from SfM[28], and then applies adaptive density control to populate empty areas. There are two forms of densitification: split and clone. Split operation is designed to split large Gaussians that represent small-scale areas in two, which corresponds to *over-reconstruction*. Clone operation aims to clone more Gaussians to sufficiently cover *under-reconstruction* region For each Gaussian G_i , 3D-GS uses the average magnitude of view-space positional gradients to determine whether to apply densitification. Specifically, for Gaussian G_i which have the pixel-space projection point $\mu_i^k = (\mu_{i,x}^k, \mu_{i,y}^k)$ under viewpoint k and corresponding loss L^k , the average view-space positional gradient



Figure 4: An example to demonstrate the difference between densification strategy of 3D-GS and AbsGS. From (b) and (c), we observe that large-scale Gaussians are used to represent cement ground, which contains fine details and indeed should be represented by many small-scale Gaussians. In (d) and (e), we show the Gaussians that satisfy densification criteria of 3D-GS and ours respectively, where identified Gaussians’ colors are set to white. When using g_i as 3D-GS, the large Gaussians that represent cement ground are not identified while our selection strategy based on \hat{g}_i can find those Gaussians.

$\nabla_{\mu_i} L$ is calculated every 100 training iterations as follows:

$$\nabla_{\mu_i} L = \frac{\sum_{k=1}^M \|\frac{\partial L^k}{\partial \mu_i^k}\|}{M} = \frac{\sum_{k=1}^M \sqrt{(\frac{\partial L^k}{\partial \mu_{i,x}^k})^2 + (\frac{\partial L^k}{\partial \mu_{i,y}^k})^2}}{M} \quad (5)$$

where M is the total number of viewpoints that Gaussian G_i participates in calculation during 100 iterations. Split for G_i is performed when it satisfies:

$$\nabla_{\mu_i} L > \tau_p \text{ and } \Sigma_i^{3d} > \tau_S \quad (6)$$

where τ_p is the the gradient threshold (default 0.0002) and τ_S is the scale threshold (default 0.01).

3.2 Gradient Collision

3D-GS relies on gradient descent to optimize the scene, so the magnitude of the gradient can reflect the quality of representation. However, the computation of $\nabla_{\mu_i} L$ includes gradient directions that are irrelevant to the representation state, weakening the effectiveness of the gradient magnitude. In this section, we analyze the negative impact of gradient directions. Specifically, there exists *gradient collision* in the calculation of $\frac{\partial L^k}{\partial \mu_{i,x}^k}$ and $\frac{\partial L^k}{\partial \mu_{i,y}^k}$, thus affect the role of $\nabla_{\mu_i} L$. To simplify the notation, we discard view k in following notations, and we use g_i , $g_{i,x}$ and $g_{i,y}$ to refer $\frac{\partial L}{\partial \mu_i}$, $\frac{\partial L}{\partial \mu_{i,x}}$ and $\frac{\partial L}{\partial \mu_{i,y}}$ respectively.

Take the x-axis gradient $g_{i,x}$ as an example. We further decompose this gradient into the sum of multiple sub-gradients contributed by each pixel:

$$g_{i,x} = \frac{\partial L}{\partial \mu_{i,x}} = \sum_{j=1}^m \frac{\partial L_j}{\partial \mu_{i,x}} \quad (7)$$

where m is the number of pixels covered by G_i , L_j is the loss computed by j -th pixel. Our key observation is that the per-pixel gradients $\frac{\partial L_j}{\partial \mu_{i,x}}$ may have different directions. The proof is as follows.

Proof. We simplify the proving goal to demonstrating that the signs of gradients may differ, which is equivalent to proving that the gradient directions are different. Per-pixel gradient $\frac{\partial L_j}{\partial \mu_{i,x}}$ can be calculated as:

$$\frac{\partial L_j}{\partial \mu_{i,x}} = \sum_{l=1}^3 \frac{\partial L_j}{\partial c_l^j} \times \frac{\partial c_l^j}{\partial \alpha_i} \times \frac{\partial \alpha_i}{\partial \mu_{i,x}} \quad (8)$$

The sign of $\frac{\partial L_j}{\partial \mu_{i,x}}$ is determined by the multiplication of signs of three individual terms.

For the first term, since L_j is \mathcal{L}_1 loss, the sign of first term $\frac{\partial L_j}{\partial c_l^j}$ depends on the comparison result of rendered and real RGB values.

For the second term $\frac{\partial c_l^j}{\partial \alpha_i}$, according to Equ.3, it can be further calculated as follows:

$$\frac{\partial c_l^j}{\partial \alpha_i} = \prod_{l=1}^{i-1} (1 - \alpha_l) c_i + \sum_{p=i+1}^N c_p \frac{\partial w_p}{\partial \alpha_i}, \quad (9)$$

$$\frac{\partial w_p}{\partial \alpha_i} = -\alpha_p \prod_{l=1, l \neq i}^{p-1} (1 - \alpha_l), \quad (10)$$

Thus, the two additions to Equ.9 have opposite signs, and the sign of $\frac{\partial c_l^j}{\partial \alpha_i}$ is uncertain. Here c_i and c_p are Gaussian colors, c_l^j is the color of the pixel.

For the third term $\frac{\partial \alpha_i}{\partial \mu_{i,x}}$, according to Equ.4, it is calculated as:

$$\frac{\partial \alpha_i}{\partial \mu_{i,x}} = \sigma(o_i) \times \frac{\partial G_i^{2d}(\mu_{i,x})}{\partial x} = \sigma(o_i) \times \frac{(\mu_{i,x} - \hat{p}_j) G_i^{2d}(\mu_{i,x})}{\sigma_1^2} \quad (11)$$

where \hat{p}_j is the coordinate of j -th pixel. Therefore, the sign of the third term $\frac{\partial \alpha_i}{\partial \mu_{i,x}}$ is determined by the relative x-axis coordinate difference $(\mu_{i,x} - \hat{p}_j)$.

Overall, the sign of first term is determined by to the rendered pixel value, the sign of second term is related all the Gaussians’ that participate in calculation, and the sign of third term is related to the projection point, so these three terms do not always have the same sign, and the per-pixel gradient $\frac{\partial L_j}{\partial \mu_{i,x}}$ may have different directions for different pixels.

We design a simple experiment to verify the above analysis, as illustrated in 3. An image is randomly selected from the *flowers* scene from Mip-NeRF360[3] and is reduced to a resolution of 100×65 in Fig. 3 (a). Then we optimize only one Gaussian to fit this image, and the final rendering result is shown in Fig. 3 (b). The overall L1 loss is large and this Gaussian leads to a typical over-reconstruction issue, in Fig. 3 (c). we show the x-axis gradient direction $\frac{\partial L_j}{\partial \mu_{i,x}}$ in Fig. 3 (d), where the pixel color means the x-axis direction of the gradient contributed by this pixel, and red is for positive x-axis direction and green for negative x-axis direction. The different directions of per-pixel gradient $\frac{\partial L_j}{\partial \mu_{i,x}}$ results the sum $\nabla_{\mu_i} L$ may

Table 1: Quantitative results on Mip-NeRF 360[1], Tanks & Temples[18], and Deep Blending[13]. All scores of the rest of the baselines are directly sourced from the original 3D-GS paper[17] to make a fair comparison. INGP-Base and INGP-Big are Instant-NGP versions with default settings and increased network size respectively. The 1st, 2nd, and 3rd-best performances are indicated by red, orange, and yellow highlights respectively.

Datasets	Mip-NeRF360				Tanks & Temples				Deep Blending			
Methods	SSIM	PSNR	LPIPS	Mem	SSIM	PSNR	LPIPS	Mem	SSIM	PSNR	LPIPS	Mem
Plenoxels	0.626	23.08	0.463	2.1GB	0.719	21.08	0.379	2.3GB	0.795	23.06	0.510	2.7GB
INGP-Base	0.671	25.30	0.371	13MB	0.723	21.72	0.330	13MB	0.797	23.60	0.423	13MB
INGP-Big	0.699	25.59	0.331	48MB	0.745	21.92	0.305	48MB	0.817	24.96	0.390	48MB
Mip-NeRF360	0.792	27.69	0.237	8.6MB	0.759	22.22	0.257	8.6MB	0.901	29.40	0.245	8.6MB
3D-GS	0.815	27.21	0.214	734MB	0.841	23.14	0.183	411MB	0.903	29.41	0.243	676MB
3D-GS*	0.809	27.36	0.220	760MB	0.842	23.64	0.179	374MB	0.897	29.57	0.240	624MB
AbsGS-0008	0.815	27.41	0.211	450MB	0.844	23.54	0.1831	202MB	0.903	29.69	0.241	380MB
AbsGS-0004	0.820	27.49	0.191	728MB	0.853	23.73	0.162	304MB	0.902	29.67	0.236	444MB

have a small-scale magnitude. Especially for large Gaussians that covering many pixels, maintaining consistent gradient directions for each pixel becomes exceptionally challenging. Consequently, the gradient magnitude fails to surpass the densification threshold τ_p , thereby hindering the split of over-reconstructed Gaussians.

3.3 Homodirectional Gradient

Based on the above analysis, we design AbsGS, which can accurately reflects the representation state and identify Gaussians in over-reconstructed regions. The overall review of our method is shown in Fig. 2. AbsGS aims to eliminate gradient collision by erasing the influence of gradient direction while retaining only the influence of gradient magnitude. Specifically, AbsGS computes the homodirectional view-space positional gradient \hat{g}_i by taking the absolute value of each component before summing:

$$\hat{g}_i = (\hat{g}_{i,x}, \hat{g}_{i,y}) \quad (12)$$

$$\hat{g}_{i,x} = \sum_{j=1}^m \left| \frac{\partial L_j}{\partial \mu_{i,x}} \right|, \quad \hat{g}_{i,y} = \sum_{j=1}^m \left| \frac{\partial L_j}{\partial \mu_{i,y}} \right| \quad (13)$$

The absolute operation constrains the gradient directions of all pixels to be in the same direction along the x and y axes, thereby avoiding gradient collision. It uses the magnitudes of the gradient components along the x and y axes to jointly express the state of representation, and finally combines these two components through the L2 norm. This value directly reflects the expression state of all the pixels covered by the Gaussian, thus accurately identifying Gaussians with subpar expression, such as over-reconstructed Gaussians. Note that the \hat{g}_i is not used in backpropagation of computation graph, it is an extra variable that only related to densification.

Fig. 4 presents a real example to compare the selected Gaussians that need densification between 3D-GS and ours. We first optimize the scene *treehill* of Mip-NeRF360 for 7000 iterations using 3D-GS. then we select over-reconstructed Gaussians by original g_i and ours homodirectional \hat{g}_i . The selected Gaussians are highlight with white, as shown in Fig. 4 (d) and (e). It shows that 3D-GS selects 69,269 Gaussians for densification but it missed most of the large Gaussians in over-reconstructed areas. In contrast, our proposed AbsGS only select 16,488 Gaussians while covering the majority of

over-reconstructed areas. This experiment effectively demonstrates that our method is better suited as the criteria for densification.

4 EXPERIMENTS

4.1 Setup

Datasets. Following 3D-GS[17], we select scenes with highly diverse capture styles, spanning from enclosed indoor environments to expansive outdoor settings without clear boundaries. Specifically, we use all 9 unbounded indoor and outdoor scenes presented in Mip-NeRF360[3], two scenes from [18] and two scenes provided by [13], totaling 13 distinct environments.

Baselines. Across all dataset, we benchmark our proposed method against multi-level hash grid based Instant-NGP[21], the current state-of-the-art NeRF-based method Mip-NeRF360, and widely-used 3D GS[17]. To ensure a fair comparison, all numerical data of these methods presented in tables are directly sourced from the original publication[17] unless otherwise specified. In addition, we observe that the scale of some scene details is smaller than the default radius threshold τ_S that used to control split operation, and thus 3D-GS is hindered in sufficient split for these regions. To further improve enhance the ability of 3D-GS. we reduced the τ_S from default 0.01 to 0.001 and retrain 3D-GS, which is denoted as 3D-GS* in following experiments. Our method AbsGS is also trained with τ_S set as 0.001. Since τ_p is a hyper-parameter that impact the behavior of AbsGS, we present the results when τ_p is set to different values. Specifically, AbsGS-0004 and AbsGS-0008 represent the results when τ_p is set to 0.0004 and 0.0008 respectively.

Implementation Details. Our experiments is measured on a single NVIDIA V100 GPU with 32GB memory. Following common practice, we stop the Gaussian densification after 15k iterations and stop training at 30k iterations. We report the novel view synthesis metrics PSNR, SSIM, and LPIPS, and we also show the number of Gaussians and the memory used to store the parameters of optimized Gaussians to demonstrate the trade-off between efficiency and memory. To highlight the effectiveness of AbsGS in addressing over-reconstruction, homodirectional gradients are only used as guidance for split operation while clone operation follows the original strategy of 3D-GS directly. We select a larger gradient threshold

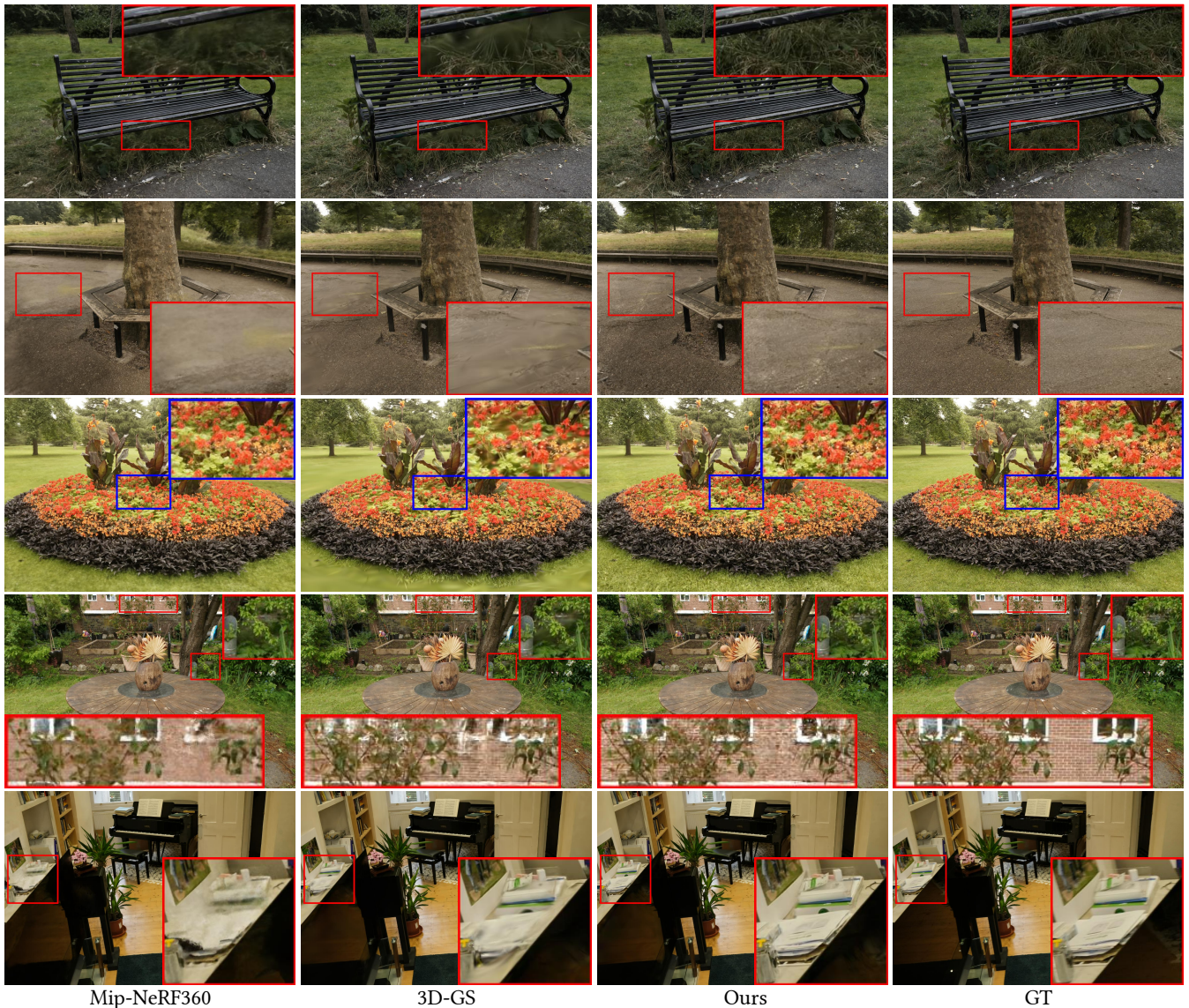


Figure 5: Qualitative comparisons of different methods on scenes from Mip-NeRF360[3] and Tanks&Temples[18] datasets. The rendering result of 3D Gaussian Splatting is blurry at regions containing high-frequency details. Our AbsGS yields significantly better rendering quality with sharper details.

τ_p for split operation since AbsGS will increase the magnitude of $\nabla_{\mu_i} L$ than that in 3D-GS.

4.2 Performance Evaluation

Quantitative Results. We report the quantitative results in Table. 1. Both AbsGS-0004 and AbsGS-0008 outperform other baselines in most cases. It’s noteworthy that our method consistently yields better result in terms of SSIM and LPIPS metrics, which capture more reliable human perception differences in images than PSNR metric. Additionally, it can be observed from the memory consumption that the effectiveness of AbsGS does not stem from an increased number of Gaussians. Compared to original 3D-GS,

AbsGS-0008 only maintains roughly half the memory consumption and AbsGS-0004 also consistently maintains lower memory, while the quantitative result of them remain highly competitive.

Qualitative Results. First, we show novel view synthesis results in Fig. 5. The results indicate that our method significantly reduces the rendering blurring phenomenon and improves rendering quality across all scenes, such as weeds under the bench and uneven concrete ground. Second, to demonstrate the effectiveness of our method in eliminating large Gaussians in over-reconstructed regions, we select *stump* scene and visualize the point clouds and ellipsoids along with the number of Gaussians in Fig. 7. We can

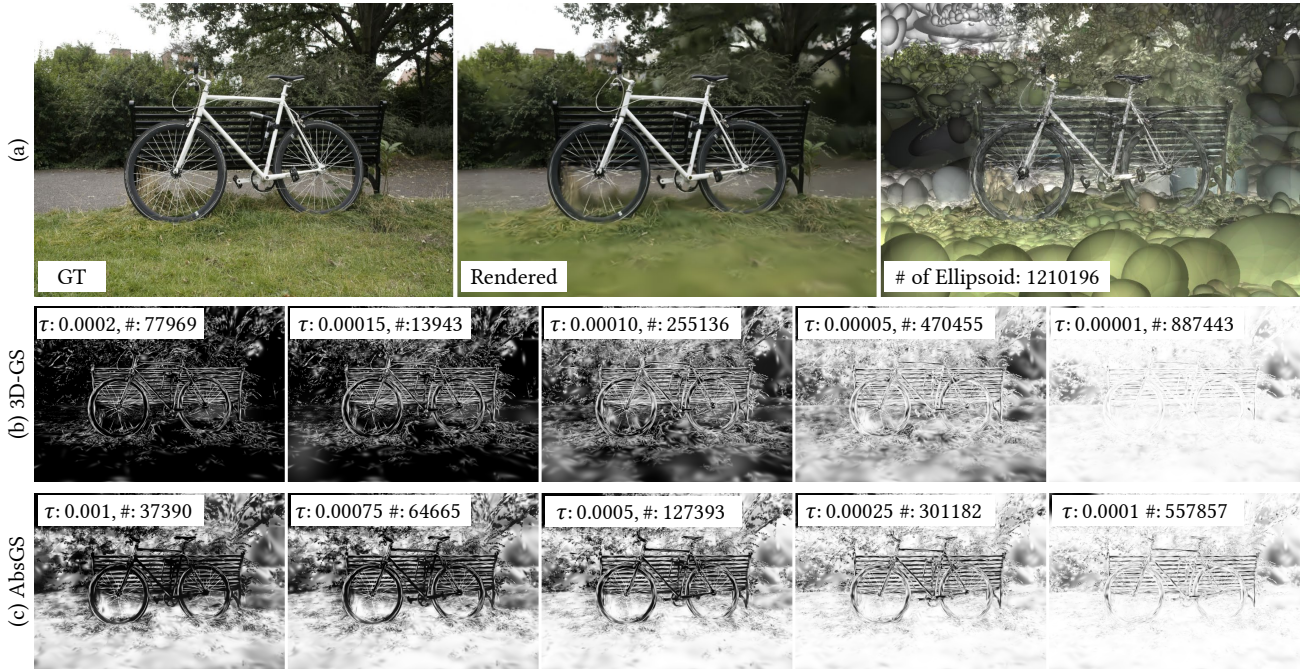


Figure 6: Comparison of identified Gaussians under different gradient thresholds. (a) The result of training the *bicycle* scene for 3000 iterations using 3D-GS with a gradient threshold of 0.0002, showing significant over-reconstruction. (b) and (c) respectively show the selection results of 3D-GS and AbsGS with different gradient thresholds at this stage. White represents Gaussians that are selected for densification while black represents those that do not. The threshold and the number of selected Gaussians are both annotated.

observe that 3D-GS exhibits over-reconstruction in areas with similar colors but rich textures, such as the grassy area, where the point cloud is very sparse and the ellipsoids are excessively large. In contrast, our method effectively utilizes smaller Gaussians for representing those areas. It is worth mentioning that the number of Gaussians of AbsGS is less than that of 3D-GS, with Abs-0008 even being less than half of 3D-GS. This indicates that our method does not rely on more Gaussians to solve the problem of over-reconstruction. Additionally, the scale threshold for Abs-0008* is set to 0.01 as same as 3D-GS, to demonstrate that the effectiveness of our method does not depend on adjusting the hyperparameter. We provide more qualitative comparisons in the supplementary material.

Ablation Studies. In this section, we conduct ablation experiments to study the impact of scale threshold τ_S and gradient threshold τ_p on our method. We present quantitative results in Tab.2. The experimental results demonstrate that lowering any of τ_p and τ_S improves rendering quality at the cost of memory. Additionally, to qualitatively illustrate the impact of τ_S on rendering quality, we show rendering result in Fig.8. The visualization demonstrates that a smaller τ_S helps to mitigate large Gaussians in over-reconstructed regions. The reason is that the scale of some scene details is smaller than τ_S ; consequently, the Gaussians on those regions that have larger radius than τ_S will not split and thus lead to blurry rendering.

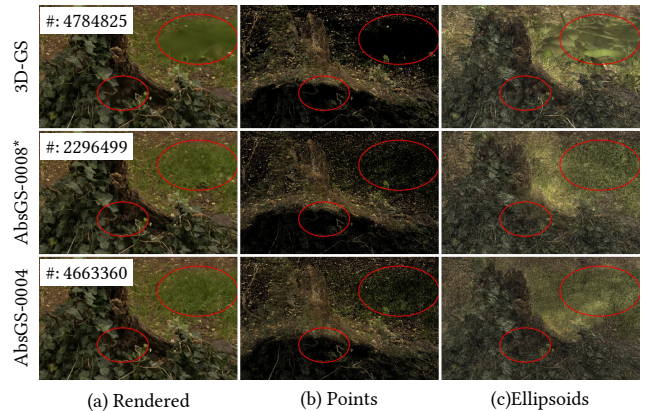


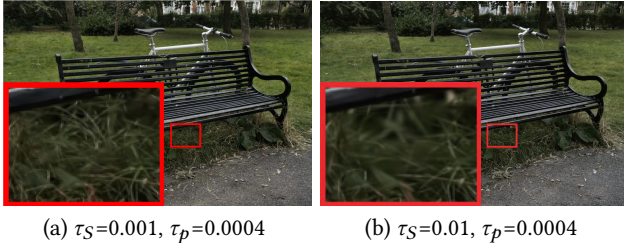
Figure 7: The visualization of rendered images, point clouds, and ellipsoids. The scale threshold for both AbsGS-0008* and 3D-GS is 0.01, while the scale threshold for AbsGS-0004 is 0.001.

4.3 Analysis

Why not solve the over-reconstruction problem by simply lowering the threshold τ_p ? Since over-reconstruction issue is caused by

Table 2: Quantitative studies for different scale threshold τ_S and gradient threshold τ_p . The 1st and 2nd performances are indicated by red and orange highlights respectively.

Datasets		Mip-NeRF360				Tanks & Temples				Deep Blending			
Methods		SSIM	PSNR	LPIPS	Mem	SSIM	PSNR	LPIPS	Mem	SSIM	PSNR	LPIPS	Mem
$\tau_S=0.01$	$\tau_p=0.0008$	0.817	27.38	0.212	374MB	0.842	23.64	0.190	159MB	0.902	29.55	0.249	265MB
$\tau_S=0.001$	$\tau_p=0.0008$	0.815	27.41	0.211	450MB	0.845	23.54	0.183	202MB	0.903	29.69	0.241	380MB
$\tau_S=0.01$	$\tau_p=0.0004$	0.820	27.52	0.202	637MB	0.8531	23.86	0.173	314MB	0.903	29.45	0.247	386MB
$\tau_S=0.001$	$\tau_p=0.0004$	0.821	27.49	0.191	728MB	0.853	23.73	0.162	304MB	0.902	29.67	0.236	444MB



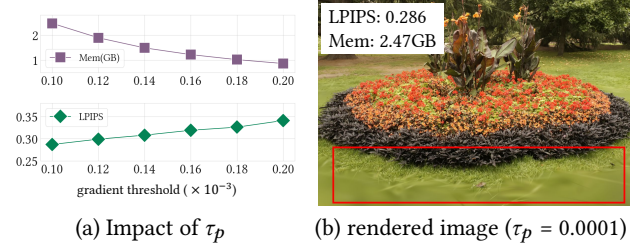
(a) $\tau_S=0.001, \tau_p=0.0004$

(b) $\tau_S=0.01, \tau_p=0.0004$

Figure 8: Comparison of results for AbsGS under different scale thresholds.

gradient collision that make it difficult for the gradient of large Gaussians to exceed threshold τ_p , a straightforward solution is lowering threshold τ_p to identify more large Gaussians in over-reconstructed regions. However, we have observed that this solution doesn't perform well in practice and leads to significant memory consumption. Fig. 9 (a) shows the LPIPS and memory consumption of 3D-GS at different thresholds τ_p in the *flowers* scene of Mip-NeRF360. The gradually increased memory requirements make the simple solution impractical for real-world applications. Additionally, we show rendering result when τ_p is set to 0.0001 in Fig. 9 (b). It's observed that the over-reconstruction issue is still evident even at the cost of 2.47GB memory. Further lowering the threshold below 0.0001 result in out of CUDA memory error when training a single V100 GPU. Above analysis reveals that simply lowering gradient threshold τ_p is impractical to eliminate over-reconstruction.

Why does addressing over reconstruction require a large amount of memory for 3D-GS while AbsGS does not? As illustrated above, directly reducing the threshold for 3D-GS τ_p is highly inefficient and impractical while our method manages to solve over-reconstruction. Next, we uncover the reasons behind it by visualizing selected Gaussians for split. In Fig. 6 (a), we train the *bicycle* scene with 3D-GS using default parameters for 3000 steps. The rendering image and ellipsoid image reveal that there are numerous over-reconstructed areas in the scene, such as lawn and trees. Fig. 6 (b) and (c) respectively show the Gaussians selected under different gradient thresholds for 3D-GS and AbsGS, with the number of selected Gaussians inset. In the case of 3D-GS with the default threshold of 0.0002, although it selected 77969 Gaussians, it did not effectively encompass over-reconstructed region. In contrast, AbsGS can select most of the over-reconstructed region by selecting only 37390 Gaussians at the threshold of 0.001. Besides this, lowering the threshold indeed allows for the selection of more over-reconstructed areas for 3D-GS, but the number of selected Gaussians increases rapidly, and the



(a) Impact of τ_p

(b) rendered image ($\tau_p = 0.0001$)

Figure 9: Comparison of results for 3D-GS under different gradient thresholds.

rate of noise in all selected Gaussians is also apparent, resulting in large memory cost. In particular, see Fig. 6 (b) and Fig. 6 (c), it can be observed that when we lower the threshold, 3D-GS selects many Gaussians that do not need split but still can not select large Gaussians in over-reconstructed regions. Above analysis demonstrates that the homodirectional gradient used by AbsGS offers a much more accurate reflection of the representation quality, leading to fewer mistakenly selected Gaussians. This fundamental distinction proves why AbsGS is more efficient than 3D-GS.

5 CONCLUSION

3D-GS has made significant strides in novel view synthesis tasks, but it frequently encounters issues such as blurriness and loss of detail stemming from over-reconstruction. This paper delves into the phenomenon of over-reconstruction and identifies gradient collision in 3D-GS's adaptive density control strategy as a primary cause. Specifically, the view-space positional gradient used in this strategy is the sum of sub-gradients of all pixels covered by a Gaussian, and these gradient directions cannot always remain consistent, leading to mutual cancellation. To tackle this challenge, our proposed AbsGS utilizes homodirectional view-space positional gradient by taking the absolute values of the x and y components of pixel-wise sub-gradients separately, eliminating the influence of direction. Extensive experiments conducted on multiple datasets against 3D-GS demonstrate the significant advantages of our method in eliminating over-reconstruction and restoring fine details. Moreover, our approach boasts lower memory consumption compared to 3D-GS, largely attributable to AbsGS's more accurate identification of over-reconstruction through the use of homodirectional gradients.

REFERENCES

- [1] Jonathan T Barron, Ben Mildenhall, Matthew Tancik, Peter Hedman, Ricardo Martin-Brualla, and Pratul P Srinivasan. 2021. Mip-nerf: A multiscale representation for anti-aliasing neural radiance fields. In *Proceedings of the IEEE/CVF*

- International Conference on Computer Vision*. 5855–5864.
- [2] Jonathan T. Barron, Ben Mildenhall, Matthew Tancik, Peter Hedman, Ricardo Martin-Brualla, and Pratul P. Srinivasan. 2021. Mip-NeRF: A Multiscale Representation for Anti-Aliasing Neural Radiance Fields. *ICCV* (2021).
 - [3] Jonathan T Barron, Ben Mildenhall, Dor Verbin, Pratul P Srinivasan, and Peter Hedman. 2022. Mip-nerf 360: Unbounded anti-aliased neural radiance fields. In *Proceedings of the IEEE/CVF Conference on Computer Vision and Pattern Recognition*. 5470–5479.
 - [4] Jonathan T. Barron, Ben Mildenhall, Dor Verbin, Pratul P. Srinivasan, and Peter Hedman. 2023. Zip-NeRF: Anti-Aliased Grid-Based Neural Radiance Fields. *ICCV* (2023).
 - [5] Anpei Chen, Zexiang Xu, Andreas Geiger, Jingyi Yu, and Hao Su. 2022. TensorRF: Tensorial Radiance Fields. In *European Conference on Computer Vision (ECCV)*.
 - [6] Hanlin Chen, Chen Li, and Gim Hee Lee. 2023. NeuSG: Neural Implicit Surface Reconstruction with 3D Gaussian Splatting Guidance. *arXiv preprint arXiv:2312.00846* (2023).
 - [7] Jaeyoung Chung, Suyoung Lee, Hyeongjin Nam, Jaerin Lee, and Kyoung Mu Lee. 2023. Lucidreamer: Domain-free generation of 3d gaussian splatting scenes. *arXiv preprint arXiv:2311.13384* (2023).
 - [8] Tianchen Deng, Yaohui Chen, Leyan Zhang, Jianfei Yang, Shenghai Yuan, Danwei Wang, and Weidong Chen. 2024. Compact 3d gaussian splatting for dense visual slam. *arXiv preprint arXiv:2403.11247* (2024).
 - [9] Yuanxing Duan, Fangyin Wei, Qiyu Dai, Yuhang He, Wenzheng Chen, and Baoquan Chen. 2024. 4D Gaussian Splatting: Towards Efficient Novel View Synthesis for Dynamic Scenes. *arXiv preprint arXiv:2402.03307* (2024).
 - [10] Sara Fridovich-Keil, Alex Yu, Matthew Tancik, Qinlong Chen, Benjamin Recht, and Angjoo Kanazawa. 2022. Plenoxels: Radiance fields without neural networks. In *Proceedings of the IEEE/CVF Conference on Computer Vision and Pattern Recognition*. 5501–5510.
 - [11] Hang Gao, Ruilong Li, Shubham Tulsiani, Bryan Russell, and Angjoo Kanazawa. 2022. Monocular dynamic view synthesis: A reality check. *Advances in Neural Information Processing Systems* 35 (2022), 33768–33780.
 - [12] Antoine Guédon and Vincent Lepetit. 2023. Sugar: Surface-aligned gaussian splatting for efficient 3d mesh reconstruction and high-quality mesh rendering. *arXiv preprint arXiv:2311.12775* (2023).
 - [13] Peter Hedman, Julien Philip, True Price, Jan-Michael Frahm, George Drettakis, and Gabriel Brostow. 2018. Deep blending for free-viewpoint image-based rendering. *ACM Transactions on Graphics* (Dec 2018), 1–15. <https://doi.org/10.1145/3272127.3275084>
 - [14] Jiarui Hu, Xianhao Chen, Boyin Feng, Guanglin Li, Liangjing Yang, Hujun Bao, Guofeng Zhang, and Zhaopeng Cui. 2024. CG-SLAM: Efficient Dense RGB-D SLAM in a Consistent Uncertainty-aware 3D Gaussian Field. *arXiv preprint arXiv:2403.16095* (2024).
 - [15] Binbin Huang, Zehao Yu, Anpei Chen, Andreas Geiger, and Shenghua Gao. 2024. 2D Gaussian Splatting for Geometrically Accurate Radiance Fields. *arXiv preprint arXiv:2403.17888* (2024).
 - [16] Ajay Jain, Ben Mildenhall, Jonathan T Barron, Pieter Abbeel, and Ben Poole. 2022. Zero-shot text-guided object generation with dream fields. In *Proceedings of the IEEE/CVF conference on computer vision and pattern recognition*. 867–876.
 - [17] Bernhard Kerbl, Georgios Kopanas, Thomas Leimkühler, and George Drettakis. 2023. 3D Gaussian Splatting for Real-Time Radiance Field Rendering. *ACM Transactions on Graphics* 42, 4 (2023).
 - [18] Arno Knapitsch, Jaesik Park, Qian-Yi Zhou, and Vladlen Koltun. 2017. Tanks and temples: Benchmarking large-scale scene reconstruction. *ACM Transactions on Graphics (TOG)* 36, 4 (2017), 1–13.
 - [19] Zhan Li, Zhang Chen, Zhong Li, and Yi Xu. 2023. Spacetime Gaussian Feature Splatting for Real-Time Dynamic View Synthesis. *arXiv preprint arXiv:2312.16812* (2023).
 - [20] Ben Mildenhall, Pratul P Srinivasan, Matthew Tancik, Jonathan T Barron, Ravi Ramamoorthi, and Ren Ng. 2021. Nerf: Representing scenes as neural radiance fields for view synthesis. *Commun. ACM* 65, 1 (2021), 99–106.
 - [21] Thomas Müller, Alex Evans, Christoph Schied, and Alexander Keller. 2022. Instant neural graphics primitives with a multiresolution hash encoding. *TOG* 41, 4 (2022), 1–15.
 - [22] Hao Ouyang, Kathryn Heal, Stephen Lombardi, and Tiancheng Sun. 2023. Text2Immersion: Generative Immersive Scene with 3D Gaussians. *arXiv preprint arXiv:2312.09242* (2023).
 - [23] Onur Özyeşil, Vladislav Voroninski, Ronen Basri, and Amit Singer. 2017. A survey of structure from motion*. *Acta Numerica* 26 (2017), 305–364.
 - [24] Keunhong Park, Utkarsh Sinha, Jonathan T Barron, Sofien Bouaziz, Dan B Goldman, Steven M Seitz, and Ricardo Martin-Brualla. 2021. Nerfies: Deformable neural radiance fields. In *Proceedings of the IEEE/CVF International Conference on Computer Vision*. 5865–5874.
 - [25] Keunhong Park, Utkarsh Sinha, Peter Hedman, Jonathan T Barron, Sofien Bouaziz, Dan B Goldman, Ricardo Martin-Brualla, and Steven M Seitz. 2021. Hypernerf: A higher-dimensional representation for topologically varying neural radiance fields. *arXiv preprint arXiv:2106.13228* (2021).
 - [26] Ben Poole, Ajay Jain, Jonathan T Barron, and Ben Mildenhall. 2022. Dreamfusion: Text-to-3d using 2d diffusion. *arXiv preprint arXiv:2209.14988* (2022).
 - [27] Christian Reiser, Songyou Peng, Yiyi Liao, and Andreas Geiger. 2021. Kilonerf: Speeding up neural radiance fields with thousands of tiny mlps. In *Proceedings of the IEEE/CVF international conference on computer vision*. 14335–14345.
 - [28] Johannes L Schonberger and Jan-Michael Frahm. 2016. Structure-from-motion revisited. In *Proceedings of the IEEE conference on computer vision and pattern recognition*. 4104–4113.
 - [29] Jiakai Sun, Han Jiao, Guangyuan Li, Zhanjie Zhang, Lei Zhao, and Wei Xing. 2024. 3DGSStream: On-the-Fly Training of 3D Gaussians for Efficient Streaming of Photo-Realistic Free-Viewpoint Videos. *arXiv preprint arXiv:2403.01444* (2024).
 - [30] Jiaxiang Tang, Zhaoxi Chen, Xiaokang Chen, Tengfei Wang, Gang Zeng, and Ziwei Liu. 2024. LGM: Large Multi-View Gaussian Model for High-Resolution 3D Content Creation. *arXiv preprint arXiv:2402.05054* (2024).
 - [31] Jiaxiang Tang, Jiawei Ren, Hang Zhou, Ziwei Liu, and Gang Zeng. 2023. Dream-gaussian: Generative gaussian splatting for efficient 3d content creation. *arXiv preprint arXiv:2309.16653* (2023).
 - [32] Matias Turkulainen, Xuqian Ren, Jaroslav Melekhov, Otto Seiskari, Esa Rahtu, and Juho Kannala. 2024. DN-Splatter: Depth and Normal Priors for Gaussian Splatting and Meshing. *arXiv preprint arXiv:2403.17822* (2024).
 - [33] Shimon Ullman. 1979. The interpretation of structure from motion. *Proceedings of the Royal Society of London. Series B. Biological Sciences* 203, 1153 (1979), 405–426.
 - [34] Can Wang, Menglei Chai, Mingming He, Dongdong Chen, and Jing Liao. 2022. Clip-nerf: Text-and-image driven manipulation of neural radiance fields. In *Proceedings of the IEEE/CVF Conference on Computer Vision and Pattern Recognition*. 3835–3844.
 - [35] Peng Wang, Lingjie Liu, Yuan Liu, Christian Theobalt, Taku Komura, and Wenping Wang. 2021. NeuS: Learning Neural Implicit Surfaces by Volume Rendering for Multi-view Reconstruction. *Advances in Neural Information Processing Systems* 34 (2021), 27171–27183.
 - [36] Yiming Wang, Qin Han, Marc Habermann, Kostas Daniilidis, Christian Theobalt, and Lingjie Liu. 2023. NeuS2: Fast learning of neural implicit surfaces for multi-view reconstruction. In *ICCV*. 3295–3306.
 - [37] Guanjun Wu, Taoran Yi, Jiemin Fang, Lingxi Xie, Xiaopeng Zhang, Wei Wei, Wenyu Liu, Qi Tian, and Xinggang Wang. 2023. 4d gaussian splatting for real-time dynamic scene rendering. *arXiv preprint arXiv:2310.08528* (2023).
 - [38] Yuxi Xiao, Nan Xue, Tianfu Wu, and Gui-Song Xia. 2023. Level-S²fM: Structure From Motion on Neural Level Set of Implicit Surfaces. In *Proceedings of the IEEE/CVF Conference on Computer Vision and Pattern Recognition*. 17205–17214.
 - [39] Yinghao Xu, Zifan Shi, Wang Yifan, Hansheng Chen, Ceyuan Yang, Sida Peng, Yujun Shen, and Gordon Wetzstein. 2024. Grm: Large gaussian reconstruction model for efficient 3d reconstruction and generation. *arXiv preprint arXiv:2403.14621* (2024).
 - [40] Chi Yan, Delin Qu, Dong Wang, Dan Xu, Zhigang Wang, Bin Zhao, and Xuelong Li. 2023. Gs-slam: Dense visual slam with 3d gaussian splatting. *arXiv preprint arXiv:2311.11700* (2023).
 - [41] Lior Yariv, Jiatao Gu, Yoni Kasten, and Yaron Lipman. 2021. Volume rendering of neural implicit surfaces. *Advances in Neural Information Processing Systems* 34 (2021), 4805–4815.
 - [42] Heng Yu, Joel Julin, Zoltán Á Milacska, Koichiro Niinuma, and László A Jeni. 2023. Cogs: Controllable gaussian splatting. *arXiv preprint arXiv:2312.05664* (2023).
 - [43] Xiaoyu Zhou, Xingjian Ran, Yajiao Xiong, Jinlin He, Zhiwei Lin, Yongtao Wang, Deqing Sun, and Ming-Hsuan Yang. 2024. GALA3D: Towards Text-to-3D Complex Scene Generation via Layout-guided Generative Gaussian Splatting. *arXiv preprint arXiv:2402.07207* (2024).
 - [44] Zi-Xin Zou, Zhipeng Yu, Yuan-Chen Guo, Yangguang Li, Ding Liang, Yan-Pei Cao, and Song-Hai Zhang. 2023. Triplane meets gaussian splatting: Fast and generalizable single-view 3d reconstruction with transformers. *arXiv preprint arXiv:2312.09147* (2023).

Supplementary Materials

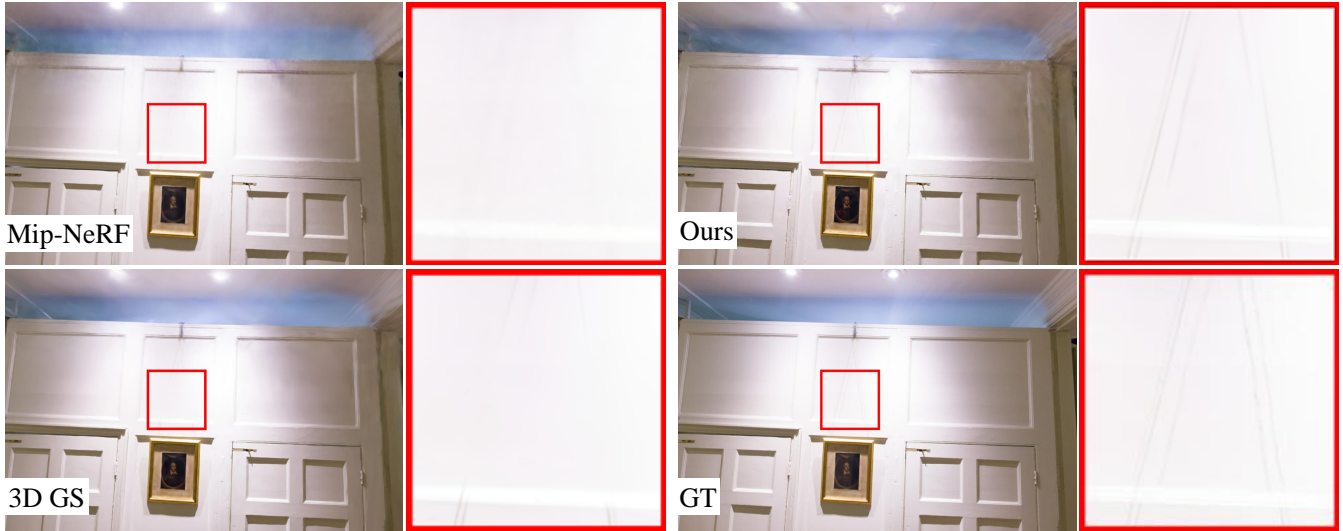


Figure 1: The visualization results of *Dr Johnson* scene from Deep Blending.

1 ADDITIONAL RESULTS

Details of the results of the experiments in the main text. Tab. 2, Tab. 3, Tab. 4, Tab. 5, Tab. 6, Tab. 7, Tab. 8 and Tab. 9 provide a breakdown of the results from Tab. 1 and 2 in the main body, presenting metrics for each scene individually, where bold indicates the best result. 3D-GS* is the model we retrained at a scale threshold of 0.001. Except for the indoor scenes of the Mip-NeRF360 dataset, our method improves on all metrics, especially the LPIPS metric. It is worth noting that compared to PSNR and SSIM, LPIPS is more in line with human eye’s perception and more sensitive to over-reconstruction. In addition, our method has significant advantages in memory consumption compared to 3D-GS. Tab. 1 shows the detailed metrics for Fig. 9 in the main body. Fig. 4

Fig. 4 displays some results of the novel view synthesis and point clouds. Our method exhibits a clear advantage in terms of point cloud complementation, particularly in over-reconstructed regions. Even with a significantly lower number of point clouds than 3D-GS in Abs-0008, it outperforms 3D-GS. The comparison for Scene *Truck* is not as obvious, primarily because this scene has a better initial point cloud quality and lower image resolution, making the original over-reconstructed regions of 3D-GS less conspicuous.

Fig. 1 illustrates the visualization results at each threshold. As the threshold increases, the over-reconstruction problem in the yellow box improves, but the area in the blue box remains almost unchanged.

Detail Comparison. Fig. 3 and 1 demonstrate the advantage of our approach in detail representation. In the TRAIN scene, 3DGS almost loses the texture details in the background. Additionally, only our method reconstructs the thin black lines in the *Dr Johnson* scene from Deep Blending.



(a) Ground truth with annotation



(b) 3D-GS



(c) Ours

Figure 3: The visualization results of *train* scene from *Tanks & Temples*. 3D-GS shows a significant over-reconstruction at the background.

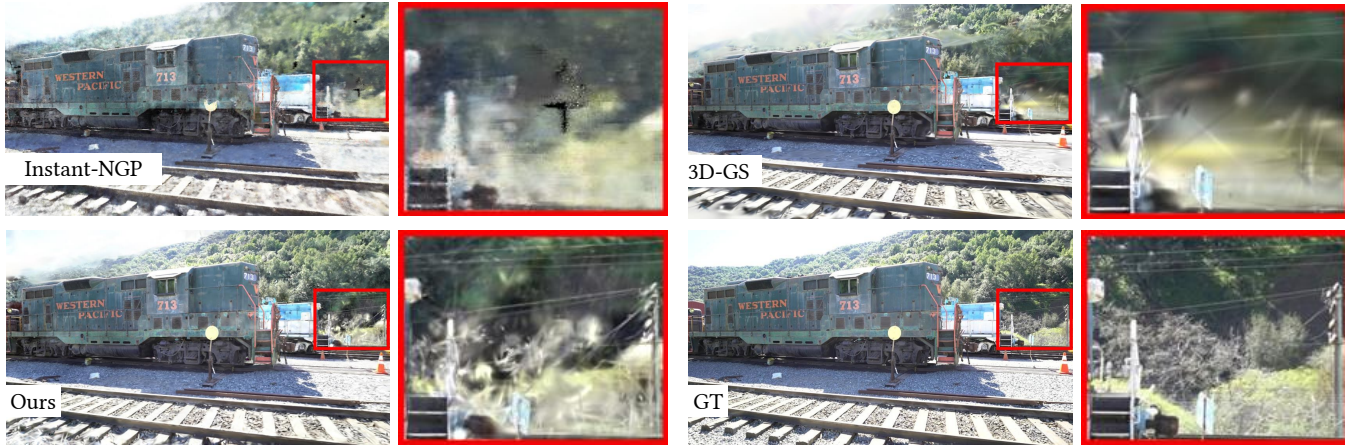


Figure 2: Qualitative comparisons of different methods on less-observed and distant regions. Our proposed AbsGS recovers more detail even when few observations are available, while other methods produce blurry and low-resolution renderings.

Impact of Scale Thresholds. Fig. 5 illustrates the comparison of the results of 3D-GS and AbsGS about scene *bicycle* under different scale thresholds (τ_s). In the main body, we demonstrate the effect of different scale thresholds on our method, illustrating how a scale threshold that is too large can limit our method’s potential. As shown in Fig. 5, 3D-GS does not eliminate over-reconstruction by lowering the scale threshold, indicating that the effectiveness of our method is not solely due to lowering the scale threshold.

In addition, lowering the threshold brings an unexpected benefit: the distribution of the point cloud is more rational. All methods in Fig. 5 exhibit more complete bicycle point clouds at small scale thresholds, particularly for bicycle spokes (the yellow circle in the Fig. 5). We explain this phenomenon with Fig. 7, where a large scale threshold limits the splitting of the Gaussian, tending to expand the Gaussian radius to represent the scene when the regions are of the same color. This benefit does not come from AbsGS. The contribution of AbsGS is to fill in the missing point clouds, see the point clouds in the yellow box in Fig. 5. Lowering the scale threshold is only effective for regions of the same color and does not fill in the empty shortcoming clouds in over-reconstructed regions.

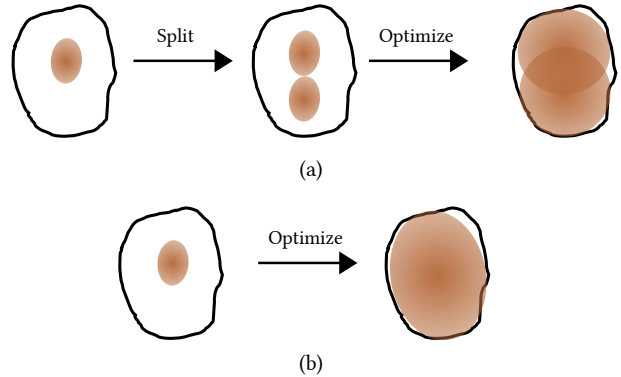


Figure 7: Effect of small-scale threshold on the distribution of point clouds in the region with a single color. (a) At small threshold, the Gaussian splits into multiple Gaussian co-expression regions, resulting in a denser point cloud. (b) Large threshold limits the splitting of the Gaussian and tends to express the whole region using a large Gaussian, resulting in a sparse point cloud.

Table 1: The results of the flowers scene under different gradient thresholds for 3D-GS.

	0.0002	0.00018	0.00016	0.00014	0.00012	0.0001
SSIM	0.600	0.611	0.618	0.624	0.628	0.636
PSNR	21.463	21.633	21.714	21.752	21.762	21.920
LPIPS	0.341	0.326	0.319	0.308	0.299	0.286
Mem	864MB	1018MB	1219MB	1487MB	1889MB	2466MB

Table 2: Per-scene quantitative results(SSIM) from the Mip-NeRF360.

		bicycle	flowers	garden	stump	treehill	room	counter	kitchen	bonsai
Plenoxels		0.496	0.431	0.606	0.523	0.509	0.8417	0.759	0.648	0.814
INGP-Base		0.491	0.450	0.649	0.574	0.518	0.855	0.798	0.818	0.890
INGP-Big		0.512	0.486	0.701	0.594	0.542	0.871	0.817	0.858	0.906
Mip-NeRF360		0.685	0.583	0.813	0.744	0.632	0.913	0.894	0.920	0.941
3D-GS		0.771	0.605	0.868	0.775	0.638	0.914	0.905	0.922	0.938
3D-GS*		0.759	0.596	0.858	0.762	0.625	0.917	0.905	0.924	0.939
S=0.01	AbsGS-0008	0.778	0.619	0.860	0.782	0.629	0.918	0.902	0.923	0.938
S=0.001	AbsGS-0008	0.773	0.612	0.863	0.770	0.621	0.919	0.906	0.925	0.941
S=0.01	AbsGS-0004	0.782	0.613	0.870	0.784	0.626	0.920	0.908	0.929	0.944
S=0.001	AbsGS-0004	0.783	0.623	0.871	0.780	0.617	0.925	0.911	0.9293	0.945

Table 3: Per-scene quantitative results(PSNR) from the Mip-NeRF360.

		bicycle	flowers	garden	stump	treehill	room	counter	kitchen	bonsai
Plenoxels		21.912	20.097	23.495	20.661	22.248	27.594	23.624	23.420	24.669
INGP-Base		22.193	20.348	24.599	23.626	22.364	29.269	26.439	28.548	30.337
INGP-Big		22.171	20.652	25.069	23.466	22.373	29.690	26.691	29.479	30.685
Mip-NeRF360		24.37	21.73	26.98	26.40	22.87	31.63	29.55	32.23	33.46
3D-GS		25.246	21.520	27.410	26.550	22.490	30.632	28.700	30.317	31.980
3D-GS*		25.12	21.439	27.11	26.457	22.385	31.35	28.93	31.312	32.11
S=0.01	AbsGS-0008	25.326	21.54	27.327	26.763	22.230	31.475	28.828	31.299	31.615
S=0.001	AbsGS-0008	25.248	21.468	27.375	26.594	22.215	31.331	28.960	31.485	32.046
S=0.01	AbsGS-0004	25.373	21.298	27.579	26.766	22.074	31.582	28.968	31.774	32.283
S=0.001	AbsGS-0004	25.290	21.347	27.487	26.711	21.986	31.614	29.031	31.621	32.323

Table 4: Per-scene quantitative results(LPIPS) from the Mip-NeRF360.

		bicycle	flowers	garden	stump	treehill	room	counter	kitchen	bonsai
Plenoxels		0.506	0.521	0.386	0.503	0.540	0.4186	0.441	0.447	0.398
INGP-Base		0.487	0.481	0.312	0.450	0.489	0.301	0.342	0.254	0.227
INGP-Big		0.446	0.441	0.257	0.421	0.450	0.261	0.306	0.195	0.205
Mip-NeRF360		0.301	0.344	0.170	0.261	0.339	0.211	0.204	0.127	0.176
3D-GS		0.205	0.336	0.103	0.210	0.317	0.220	0.204	0.129	0.205
3D-GS*		0.214	0.341	0.113	0.220	0.337	0.220	0.203	0.129	0.206
S=0.01	AbsGS-0008	0.199	0.312	0.118	0.212	0.308	0.218	0.218	0.131	0.207
S=0.001	AbsGS-0008	0.194	0.310	0.118	0.215	0.309	0.217	0.203	0.130	0.202
S=0.01	AbsGS-0004	0.186	0.295	0.104	0.202	0.297	0.216	0.198	0.124	0.194
S=0.001	AbsGS-0004	0.171	0.270	0.100	0.195	0.278	0.200	0.189	0.121	0.190

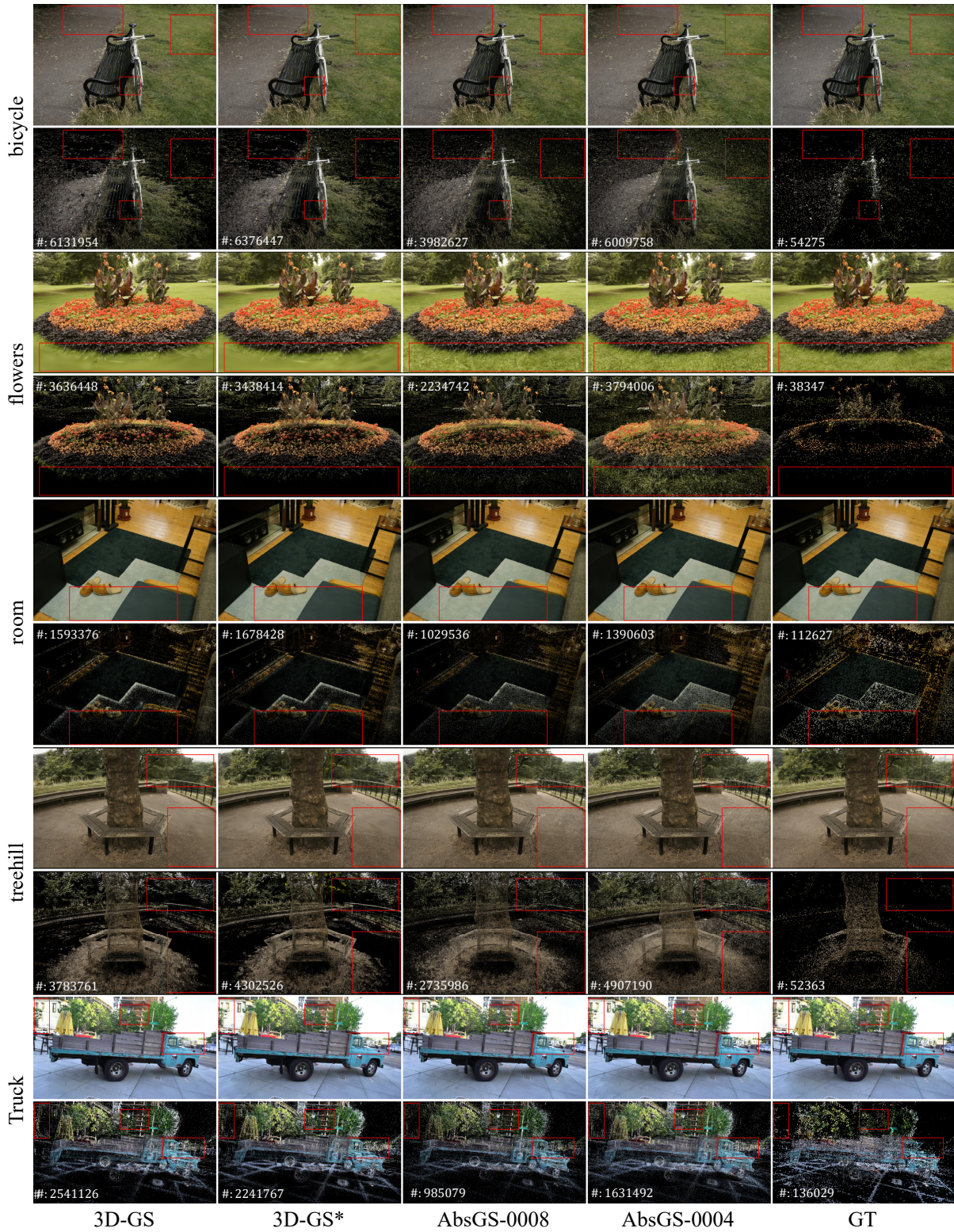


Figure 4: Comparison of novel view synthesis quality and point clouds in different scenes. Ground truth point cloud represents the point cloud of SfM



Figure 5: Comparison of 3D-GS and AbsGS results about scene *bicycle* under different thresholds



Figure 6: Rendered images of 3D-GS on *flowers* scene with different gradient thresholds. From left to right, the threshold gradually decreases.

Table 5: Per-scene memory consumption(MB) from the Mip-NeRF360.

		bicycle	flowers	garden	stump	treehill	room	counter	kitchen	bonsai
3D-GS*		1508	813	1073	1100	1018	397	257	412	259
S=0.01	AbsGS-0008	699	439	506	543	543	198	125	183	132
S=0.001	AbsGS-0008	941	529	584	601	647	243	145	213	150
S=0.01	AbsGS-0004	1156	751	932	1021	962	234	192	249	234
S=0.001	AbsGS-0004	1421	897	900	1103	1161	329	225	274	241

Table 6: Per-scene quantitative results(SSIM) from the Tanks & Temples and Deep Blending.

		Truck	Train	Dr Johnson	Playroom
Plenoxels		0.774	0.663	0.787	0.802
INGP-Base		0.779	0.666	0.839	0.754
INGP-Big		0.800	0.689	0.854	0.779
Mip-NeRF360		0.857	0.660	0.901	0.900
3D-GS		0.879	0.802	0.899	0.906
3D-GS*		0.877	0.808	0.895	0.898
S=0.01	AbsGS-0008	0.877	0.807	0.9009	0.903
S=0.001	AbsGS-0008	0.882	0.808	0.899	0.907
S=0.01	AbsGS-0004	0.886	0.820	0.900	0.9072
S=0.001	AbsGS-0004	0.888	0.818	0.898	0.907

Table 7: Per-scene quantitative results(PSNR) from the Tanks & Temples and Deep Blending.

		Truck	Train	Dr Johnson	Playroom
Plenoxels		23.221	23.221	23.142	22.980
INGP-Base		23.260	20.170	27.750	19.483
INGP-Big		23.383	20.456	28.257	21.665
Mip-NeRF360		24.912	19.523	29.140	29.657
3D-GS		25.187	21.097	28.766	30.044
3D-GS*		25.430	21.851	29.195	29.935
S=0.01	AbsGS-0008	25.449	21.819	29.155	29.953
S=0.001	AbsGS-0008	25.57	21.51	29.195	30.19
S=0.01	AbsGS-0004	25.702	22.010	28.930	29.967
S=0.001	AbsGS-0004	25.735	21.721	29.197	30.141

Table 8: Per-scene quantitative results(LPIPS) from the Tanks & Temples and Deep Blending.

		Truck	Train	Dr Johnson	Playroom
Plenoxels		0.335	0.422	0.521	0.499
INGP-Base		0.274	0.386	0.381	0.465
INGP-Big		0.249	0.360	0.352	0.428
Mip-NeRF360		0.159	0.354	0.237	0.252
3D-GS		0.148	0.218	0.244	0.241
3D-GS*		0.149	0.209	0.241	0.239
S=0.01	AbsGS-0008	0.156	0.224	0.249	0.248
S=0.001	AbsGS-0008	0.152	0.214	0.242	0.240
S=0.01	AbsGS-0004	0.131	0.193	0.240	0.232
S=0.001	AbsGS-0004	0.116	0.157	0.156	0.179

Table 9: Per-scene memory consumption(MB) from the Tanks & Temples and Deep Blending.

		Truck	Train	Dr Johnson	Playroom
3D-GS*		530	218	744	504
S=0.01	AbsGS-0008	204	115	328	201
S=0.001	AbsGS-0008	233	170	523	237
S=0.01	AbsGS-0004	419	210	457	316
S=0.001	AbsGS-0004	386	222	558	330